CrossMark

Multi-component Cahn–Hilliard system with different boundary conditions in complex domains

Yibao Li [a], Jung-Il Choi [b],*, Junseok Kim [c]

[a] *School of Mathematics and Statistics, Xi'an Jiaotong University, Xi'an 710049, China*
[b] *Department of Computational Science and Engineering, Yonsei University, Seoul 03722, Republic of Korea*
[c] *Department of Mathematics, Korea University, Seoul 02841, Republic of Korea*

A R T I C L E   I N F O

A B S T R A C T

We propose an efficient phase-field model for multi-component Cahn–Hilliard (CH) systems in complex domains. The original multi-component Cahn–Hilliard system with a fixed phase is modified in order to make it suitable for complex domains in the Cartesian grid, along with contact angle or no mass flow boundary conditions on the complex boundaries. The proposed method uses a practically unconditionally gradient stable nonlinear splitting numerical scheme. Further, a nonlinear full approximation storage multigrid algorithm is used for solving semi-implicit formulations of the multi-component CH system, incorporated with an adaptive mesh refinement technique. The robustness of the proposed method is validated through various numerical simulations including multi-phase separations via spinodal decomposition, equilibrium contact angle problems, and multi-phase flows with a background velocity field in complex domains.

© 2016 Elsevier Inc. All rights reserved.

1. Introduction

The Cahn–Hilliard (CH) equation was originally derived for spinodal decomposition [1,2] and has been widely adopted to model many other physical phenomena such as mixing [3], contact angle and wetting problems [4,5], liquid–liquid jets [6–9], solid tumor growth [10,11], image processing [12], and surface/volume reconstruction [13]. The generalized CH equation for multi-component systems was first proposed by Fontaine [14] and Morral and Cahn [15] for modeling the dynamic behavior of alloy materials exhibiting multiple phases in their micro-structures. Many researchers have investigated the mathematical modeling of multi-component CH systems. For example, Hoyt [16] extended the CH continuum theory of nucleation to multi-component solutions. Elliott and Luckhaus [17] obtained a global existence result under constant mobility and specific assumptions. Eyre [18] studied the differences between multi-component and binary alloys and discussed the equilibrium and dynamic behavior of multi-component systems. Elliot and Garcke [19] proved the global existence of multi-component systems when the mobility matrix depends on the concentration. Maier-Paape et al. [20] explained the initial-stage phase separation process in multi-component CH systems through spinodal decomposition.

One of the main problems in numerically solving the CH system is associated with the characteristics of the fourth-order spatial derivatives in the system, which makes the finite-difference stencils extremely large and introduces a severe time step restriction due to numerical instability. To overcome this problem, various numerical approaches have been developed

* Corresponding author.
  E-mail addresses: yibaoli@xjtu.edu.cn (Y. Li), jic@yonsei.ac.kr (J.-I. Choi), cfdkim@korea.ac.kr (J. Kim).
  URLs: http://gr.xjtu.edu.cn/web/yibaoli (Y. Li), http://cse.yonsei.ac.kr (J.-I. Choi), http://elie.korea.ac.kr/~cfdkim (J. Kim).

for a large number of components. Lee and Kim [21] proposed an efficient nonlinear multigrid method to solve a discrete multi-component CH system with second-order temporal accuracy. This approach can significantly reduce the required computer memory and CPU time because it only needs to solve a $2(N-1) \times 2(N-1)$ matrix inversion in an N-component CH system. Here, N is the number of components. Subsequently, Lee et al. [22] proposed a practically unconditionally gradient stable conservative nonlinear numerical scheme for converting an N-component CH system into a system of $N-1$ binary CH equations. Although the two above-mentioned methods are efficient in terms of computational costs, they are limited to multi-phase CH systems in a simple rectangular domain.

Recently, many researchers have studied the Cartesian grid method and the finite-volume method for solving the Poisson equation [23,24] and the binary CH equation [25,26] in an irregular domain. Cartesian grid embedded (or immersed) boundary methods [27–29] have an advantage compared to unstructured or body-conformal grid methods because of the simplicity in the grid generation. However, Cartesian methods require special treatments such as immersed boundary techniques for predicting accurate phase distributions near complex boundaries. Furthermore, their extension to the adaptive mesh refinement (AMR) framework involves challenging issues in accurately imposing a contact boundary condition at complex boundaries with mesh refinements. Since AMR is able to provide spatial multi-resolution in a computational domain, it is a good choice for increasing computational efficiency [30–33]. However, AMR implementation in an irregular domain could be difficult for different boundary conditions.

In this paper, we propose an efficient numerical procedure for solving multi-component CH systems in complex domains. The complex domain is first defined with a Cartesian grid and then can be determined by a signed distance function and a hyperbolic tangent profile. We modify the original multi-component CH system in a complex domain as a multi-component CH system with a fixed phase that mimics the complex boundary in the Cartesian grid. Then, by considering a hyperbolic tangent profile for the equilibrium phase interface at the complex boundaries, we recast the multi-component CH system with no mass flow or contact angle boundary conditions to satisfy the surface energy formulation. The proposed method is implemented in the AMR framework with the gradient stable nonlinear splitting numerical scheme [22] in order to eliminate high-order time step stability constraints. We use a nonlinear full approximation storage multigrid algorithm for solving the multi-component CH system. Further, we perform various numerical simulations of multi-component CH systems in complex domains such as multi-phase separations via spinodal decomposition, equilibrium contact angle problems, and multi-phase flows with a background velocity field in order to demonstrate the robustness and accuracy of the proposed method.

The remainder of this paper is organized as follows. The proposed phase-field model for a multi-component CH system in a complex domain is formulated in Section 2. The implementation of the proposed model in the AMR framework is described in Section 3. Various numerical simulation results for multi-component CH systems are presented in Section 4. Finally, the paper is concluded in Section 5.

2. Governing equations

2.1. Original multi-component Cahn–Hilliard system

We consider a system of an N-component mixture in a domain $\Omega \subset \mathbf{R}^d$ ($d = 1, 2, 3$). Let $c_i = c_i(\mathbf{x}, t)$ for $i = 1, \ldots, c_N$ be the concentration of each component in the mixture as a function of space and time. Thus, the admissible states belong to the Gibbs N-simplex,

$$G := \left\{ \mathbf{c} \in \mathbb{R}^N \,\middle|\, \sum_{i=1}^N c_i = 1, \ 0 \le c_i \le 1 \right\}. \tag{1}$$

Let $\mathbf{c} = (c_1, c_2, \ldots, c_N)$ be a vector-valued phase field; the Helmholtz free energy can be written as

$$\mathcal{E}(\mathbf{c}) = \int_\Omega \left(F(\mathbf{c}) + \frac{\epsilon^2}{2} \sum_{i=1}^N |\nabla c_i|^2 \right) d\mathbf{x}, \tag{2}$$

where $F(\mathbf{c}) = \sum_{i=1}^N c_i^2 (1 - c_i)^2 / 4$ is the Helmholtz free energy per unit volume of a homogeneous system of composition $\mathbf{c}$ and $\epsilon > 0$ is the gradient energy coefficient. The time evolution of $\mathbf{c}$ is governed by the energy changes with respect to the $\dot{H}^{-1}$ inner product. Note that the Hilbert space $\dot{H}$ is chosen as a zero-average subspace with a bounded linear mapping $\dot{H}^{-1}$ on the zero-average space. The multi-component CH system takes the following form [22]:

$$\frac{\partial c_i}{\partial t} = \nabla \cdot (M(\mathbf{c}) \nabla \mu_i), \tag{3}$$

$$\mu_i = f(c_i) + \beta(c_i) - \epsilon^2 \Delta c_i, \quad \text{for } i = 1, \ldots, N, \tag{4}$$

where

$$M(\mathbf{c}) = \sum_{i=1}^N \sum_{j>i}^N (c_i^2 c_j^2), \quad f(c_i) = \frac{\partial F(\mathbf{c})}{\partial c_i}, \text{ and } \beta(c_i) = -\frac{1}{N} \sum_{j=1}^N \frac{\partial F(\mathbf{c})}{\partial c_j}. \tag{5}$$
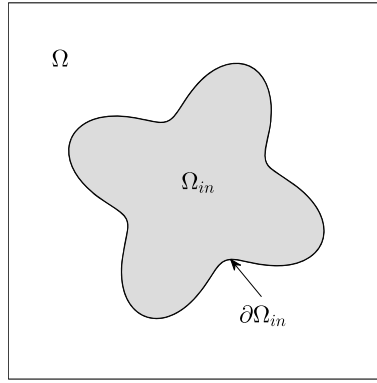
Fig. 1. Complex domain Ω_{in}.

Here, $M(\mathbf{c})$ is a concentration-dependent mobility, μ_i is a chemical potential, and $f(c_i)$ is simplified as $c_i(c_i - 0.5)(c_i - 1)$. In the present study, the Lagrangian undetermined multiplier $\beta(c_i)$ used in Eq. (5) is based on the form in Refs. [16,17,21,34] for holding the additional constraint in Eq. (1), which implies that $\frac{\partial}{\partial t} \Sigma_{i=1}^N c_i(\mathbf{x}, t) = 0$ for any time t and space $\mathbf{x}$. Substituting Eq. (4) into Eq. (3) and summing parts by parts yield $\sum_{i=1}^N f(c_i) + \sum_{i=1}^N \beta(c_i) = 0$. Thus, a simple choice of $\beta(c_i)$ leads to Eq. (5). The zero Neumann boundary conditions [22] are imposed at the domain boundary ($\partial\Omega$) for mixture concentration in the N-component CH system in order to maintain the mass conservation:

$$\nabla c_i \cdot \mathbf{n} = \nabla \mu_i \cdot \mathbf{n} = 0 \quad \text{on } \partial\Omega, \tag{6}$$

where $\mathbf{n}$ is the unit normal vector to $\partial\Omega$. For the Gibbs N-simplex in Eq. (1), we only need to solve Eqs. (3) and (4) with $N-1$ components and update $c_N = 1 - \sum_{i=1}^{N-1} c_i$ for the Nth component in the CH system.

2.2. Modified multi-component Cahn–Hilliard system in a complex domain

Numerical simulations for a multi-component CH system in a complex domain need to accurately predict the mixture concentrations at the boundaries of the domain. Although a body-conformal grid for the complex domain allows boundary conditions to be accurately imposed, it requires non-trivial efforts for grid generation and complicates the computation owing to the burden of grid transformation. When the CH equation is solved in the Cartesian grid, special treatments such as immersed boundary techniques are required for resolving the complex domain. Here, we propose a multi-component CH system suitable for complex domains in the Cartesian grid, along with two types of boundary conditions (no mass flow and contact angle boundary conditions) on the complex boundaries. The no mass flow boundary condition implies that the boundary condition is undetermined (or unknown) under the constraint that an N-component mixture cannot penetrate into the boundaries. The Neumann boundary condition is also considered, which is defined with a special contact angle of 90°. Compared to other efficient algorithms for simulations in complex domains, the proposed numerical scheme has an additional advantage in that it can be straightforwardly applied to adaptive mesh refinement.

Let Ω_{in} be a complex domain in Ω, as shown in Fig. 1. We consider the complex domain as a fixed component, $c_0(\mathbf{x})$, satisfying

$$c_0(\mathbf{x}) = \begin{cases} 1, & \text{if } \mathbf{x} \in \Omega_{in}, \\ 0, & \text{if } \mathbf{x} \in \Omega - \Omega_{in}. \end{cases} \tag{7}$$

An N-component CH system with a complex domain can be extended to the Gibbs $(N+1)$-simplex as an $(N+1)$-component CH system,

$$\hat{G} := \left\{ \mathbf{c} \in \mathbb{R}^{N+1} \,\middle|\, \sum_{i=0}^N c_i = 1, \ 0 \leq c_i \leq 1 \right\}. \tag{8}$$

Since the fixed phase $c_0(\mathbf{x})$ for the complex domain cannot mix with other phases, this phase can be determined by imposing a proper boundary treatment. Thus, the CH equation can be modified as

$$\frac{\partial c_i}{\partial t} = \nabla \cdot (\hat{M}(\mathbf{c}) \nabla \mu_i), \tag{9}$$

$$\mu_i = f(c_i) + \hat{\beta}(c_i) - \epsilon^2 \Delta c_i, \quad \text{for } i = 1, \ldots, N-1, \tag{10}$$

where

$$\hat{M}(\mathbf{c}) = \sum_{i=0}^N \sum_{j>i}^N (c_i^2 c_j^2) \text{ and } \hat{\beta}(c_i) = -c_i \sum_{j=0}^N f(c_j). \tag{11}$$
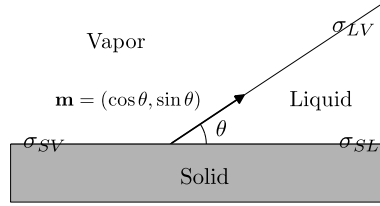
Fig. 2. Definitions of dihedral angles at the junction of the three phases.

Note that we obtain the phase $c_i(\mathbf{x})$ for $i = 1, \ldots, N-1$ by solving Eqs. (9) and (10), while the phase $c_0(\mathbf{x})$ is fixed and $c_N(\mathbf{x})$ is directly calculated by Eq. (8).

On the other hand, the dihedral contact angle is formed at the interface among the three phases or between the liquid and vapor phases and a solid surface. If the boundary condition is explicitly defined as a specific contact angle, the wetting condition can be expressed in terms of the microscale contact angle θ. In the surface energy formulation, the condition yields Young's equation [35]:

$$\sigma_{VL} \cos\theta = \sigma_{VS} - \sigma_{LS}, \tag{12}$$

where σ_{VL}, σ_{VS}, and σ_{LS} are the surface tensions for vapor–liquid, vapor–solid, and liquid–solid, respectively, as shown in Fig. 2. Thus, in the multi-component CH system, the boundary condition,

$$\nabla c_i \cdot \mathbf{n}_s = -|\nabla c_i| \cos\theta = -c_i(c_i - 1) \cos\theta/(\sqrt{2}\epsilon) \tag{13}$$

should be satisfied on the solid domain boundary. Here, $\mathbf{n}_s = \nabla c_0/|\nabla c_0|$ denotes the unit normal vector to $\partial\Omega_{in}$. If the equilibrium interfacial profile takes a hyperbolic tangent function, we can use $|\nabla c_i| = c_i(1 - c_i)/(\sqrt{2}\epsilon)$ defined in [36]. Since $\nabla c_i \cdot \mathbf{n}_s = \nabla c_i \cdot \nabla c_0/|\nabla c_0|$ on $\partial\Omega_{in}$, Eq. (13) yields

$$\epsilon^2 \nabla c_0 \cdot \nabla c_i + \epsilon c_i(c_i - 1)|\nabla c_0| \cos\theta/\sqrt{2} = 0. \tag{14}$$

Considering the boundary condition in Eq. (14) and the fixed phase condition in Eq. (7), the CH system is then modified as

$$\frac{\partial c_i}{\partial t} = \nabla \cdot ((1 - c_0)M(\mathbf{c})\nabla\mu_i), \text{ for } i = 1, \ldots, N-1 \tag{15}$$

$$\mu_i = f(c_i) + \beta(c_i) + \epsilon c_i(c_i - 1)|\nabla c_0| \cos\theta/\sqrt{2} - \epsilon^2 \nabla \cdot ((1 - c_0)\nabla c_i), \tag{16}$$

on the entire domain Ω. Further, we can directly compute $c_N = 1 - \sum_{i=0}^{N-1} c_i$ using Eq. (8). Here, the fixed phase condition in Eq. (7) is used as a Heaviside function indicating the fixed phase or non-fixed phases in formulating Eq. (15). It should be noted that Eqs. (15) and (3) are equivalent because $c_0 = 0$ in the liquid domain ($\Omega - \Omega_{in}$). Moreover, Eq. (15) yields $\partial c_i/\partial t = 0$ because $c_0 = 1$ in the solid domain (Ω_{in}), which means that c_i remains zero for any value of μ_i. By starting from Eq. (4) in the original model, the chemical potential μ_i can be given as

$$\mu_i = f(c_i) + \beta(c_i) - \epsilon^2 \nabla \cdot ((1 - c_0)\nabla c_i) - \epsilon^2 \nabla c_0 \cdot \nabla c_i - \epsilon^2 c_0 \Delta c_i. \tag{17}$$

Incorporating the boundary condition in Eq. (14) and the fixed phase condition in Eq. (7), the chemical potential in Eq. (17) can be approximated by that in Eq. (16) for the following reasons. Because $c_0 = 0$ in the liquid domain ($\Omega - \Omega_{in}$), Eqs. (16) and (17) are equivalent. Since Eq. (15) can be deduced to $\partial c_i/\partial t = 0$ in the solid domain (Ω_{in}), μ_i can be given as any value. According to the boundary condition in Eq. (14) on the solid boundary ($\partial\Omega_{in}$), $\epsilon^2 \nabla c_0 \cdot \nabla c_i$ in Eq. (17) can be replaced by $-\epsilon c_i(c_i - 1)|\nabla c_0| \cos\theta/\sqrt{2}$. Since the last term in Eq. (17) becomes approximately zero as $c_0 \to 0$, we ignore the effect of the last term on the boundary. This implies that the contact angle boundary condition can be exactly held as $c_0 \to 0$. Although Eq. (16) may induce the interface of the phases to significantly overlap the solid boundary, the numerical tests in Section 4.2.2 indicate that the proposed form accurately captures an equilibrium phase interface contacting a solid boundary.

2.3. Diffusion process for complex domains

The fixed phase $c_0(\mathbf{x})$ is set to one and zero inside and outside the complex domain, respectively, which implies that the fixed phase is defined as a sharp interface. However, in a finite-difference method, it is difficult to accurately calculate ∇c_0 unless a higher-order method is applied. Therefore, instead of considering the sharp interface, we consider a diffusion deformable interface in a discrete domain, which is more suitable for the AMR framework. In this approach, we define $c_0(\mathbf{x})$ as

$$c_0(\mathbf{x}) = 0.5 + 0.5 \tanh(d(\mathbf{x})/(2\sqrt{2}\epsilon)), \tag{18}$$
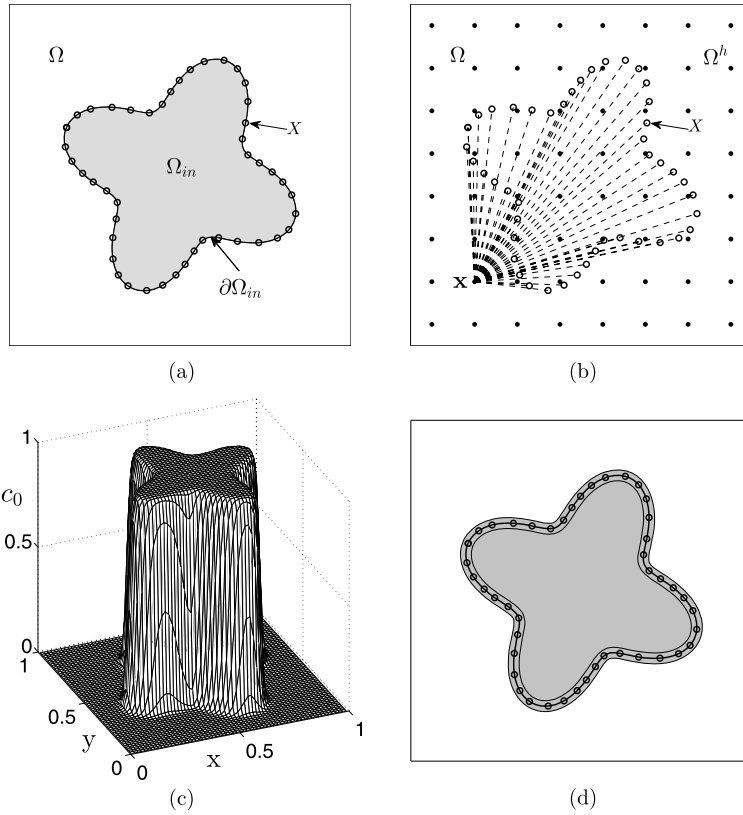
Fig. 3. (a) Schematic illustration of a complex solid region whose boundary is shown as a line with circles, (b) definition of signed discrete distance function $d(\mathbf{x})$, (c) mesh plot of $c_0(\mathbf{x})$ defined in Eq. (18), and (d) a transition region where transaction boundaries (solid lines) are extracted using $c_0(\mathbf{x}) = 0.5$.

where ϵ is the thickness of the solid boundary transition layer and $d(\mathbf{x})$ is a signed distance function from $\mathbf{x}$ in Ω to the Cartesian grid $\mathbf{X}$ in $\partial\Omega_{in}$. The sign of $d(\mathbf{x})$ is positive if $\mathbf{x}$ is inside Ω_{in} and negative otherwise. Fig. 3 (a) shows a solid region represented by a set of boundary points $\mathbf{X}$ in a domain Ω. The signed discrete distance functions $d(\mathbf{x})$ are computed in a discrete domain Ω_h (see Fig. 3 (b)), where the length of the dash-dot line segment represents the distance from $\mathbf{x}$ in Ω_h to $\mathbf{X}$ in $\partial\Omega_{in}$. Fig. 3 (c) shows the mesh plot of $c_0(\mathbf{x})$ defined in Eq. (18). Fig. 3 (d) shows the extracted transition boundaries by contour lines with $c_0(\mathbf{x}) = 0.5$, along with the solid boundary. The signed distance approach captures the shape of a complex solid boundary effectively and provides a reliable solid boundary transition region with uniformly distributed thickness of the transition layer.

3. Numerical procedure

Let $\Omega = (a, b) \times (c, d)$ be a computational domain in two-dimensional space. Let $x_i = a + (i - 0.5)h$, $y_j = c + (j - 0.5)h$, $0 \le i \le N_x + 1$, $0 \le j \le N_y + 1$, where N_x and N_y are positive even integers and $h = (b - a)/N_x = (d - c)/N_y$ is the uniform mesh size. The discrete domain is then defined as $\Omega^h = \{(x_i, y_j) | \ 1 \le i \le N_x, \ 1 \le j \le N_y\}$. Let $c_{r,ij}^n$ be an approximation of $c_r(x_i, y_j, n\Delta t)$, where $\Delta t = T/N_t$ is the time step, T is the final time, and N_t is the total number of computational time steps. A semi-implicit formulation for the multi-component CH equations in Eqs. (9) and (10) can be written as [21]

$$\frac{c_{r,ij}^{n+1} - c_{r,ij}^n}{\Delta t} = \nabla_d \cdot (\hat{M}(\mathbf{c}_{ij}^n)\nabla_d \mu_{r,ij}^{n+1}), \tag{19}$$

$$\mu_{r,ij}^{n+1} = f(c_{r,ij}^{n+1}) + 0.25 c_{r,ij}^{n+1} - 0.25 c_{r,ij}^n + \hat{\beta}_{ij} - \epsilon^2 \Delta_d c_{r,ij}^{n+1}. \tag{20}$$

The second-order central difference scheme in space is used for discretization of Eqs. (19) and (20), and the Laplacian terms are defined as

$$\nabla_d \cdot (\hat{M}(\mathbf{c}_{ij}^n)\nabla_d \mu_{r,ij}^{n+1}) = \frac{\hat{M}(\mathbf{c}_{i+1/2,j}^n)(\mu_{r,i+1,j}^{n+1} - \mu_{r,ij}^{n+1}) - \hat{M}(\mathbf{c}_{i-1/2,j}^n)(\mu_{r,ij}^{n+1} - \mu_{r,i-1,j}^{n+1})}{h^2}$$
$$+ \frac{\hat{M}(\mathbf{c}_{i,j+1/2}^n)(\mu_{r,i,j+1}^{n+1} - \mu_{r,ij}^{n+1}) - \hat{M}(\mathbf{c}_{i,j-1/2}^n)(\mu_{r,ij}^{n+1} - \mu_{r,i,j-1}^{n+1})}{h^2}, \tag{21}$$
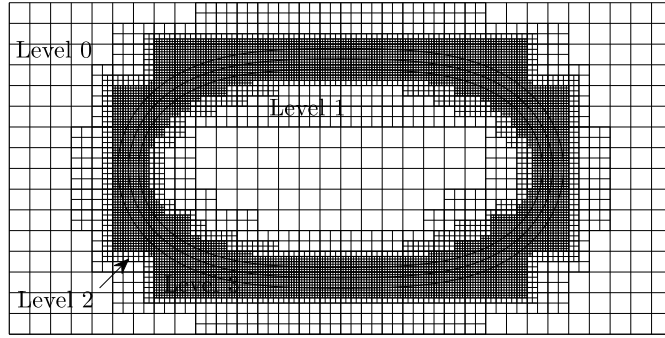
Fig. 4. Block-structured local refinement with the level $l^* = 3$. The contours represent the interface of the phase-field, i.e., $c \in [0.01, 0.99]$.

$$\Delta_d c_{r,ij}^{n+1} = \frac{c_{r,i+1,j}^{n+1} + c_{r,i-1,j}^{n+1} - 4c_{r,ij}^{n+1} + c_{r,i,j+1}^{n+1} + c_{r,i,j-1}^{n+1}}{h^2}, \tag{22}$$

where $\mathbf{c}_{i+1/2,j}^n$ is the average value of $\mathbf{c}_{i+1,j}^n$ and $\mathbf{c}_{ij}^n$. The other terms can be defined in a similar manner. The resulting nonlinear system of Eqs. (19) and (20) is solved efficiently using a nonlinear multigrid method. This nonlinear system is proven to be unconditionally gradient stable in [31].

3.1. Dynamic adaptive mesh refinement algorithm

For an adaptive mesh refinement (AMR) algorithm, we consider a hierarchy of increasingly finer grids, $\Omega_{l+1}, \ldots, \Omega_{l+l^*}$, restricted to increasingly smaller subdomains, while the last hierarchy of global grids is $\Omega_0, \Omega_1, \ldots, \Omega_l$. In other words, we consider a hierarchy of grids, $\Omega_0, \Omega_1, \ldots, \Omega_{l+0}, \Omega_{l+1}, \ldots, \Omega_{l+l^*}$. Here, we denote Ω_{l+0} as level zero, Ω_{l+1} as level one, and so on. The construction of the multi-level mesh begins at the zero-level grid. Grids of finer resolutions are added at level one to cover those grid points at level zero where refinements are flagged. This process continues in the same manner until level l^* is reached. Moreover, the grid spacing h_k at level k is related to that at the next level $(k+1)$ as $h_k = 2h_{k+1}$. Fig. 4 shows a schematic illustration of a set of finer grids with four levels ($l^* = 3$), where the AMR is implemented by uniformly subdividing each mother cell into four daughter cells. Here, the contour lines represent the interface of the phase field, i.e., $c \in [0.01, 0.99]$.

3.1.1. Creation of hierarchical grid

There are many possible criteria for determining a region where grid refinement is necessary. For example, the gradient and the distributions of the order parameter provide an indicator for grid refinement [37,38]. In the present implementation, the grid is dynamically adapted on the basis of an undivided gradient $|\nabla_u M|^k$, which is defined as

$$|\nabla_u M|_{ij}^k = \sqrt{(M_{i+1,j}^k - M_{i-1,j}^k)^2 + (M_{i,j+1}^k - M_{i,j-1}^k)^2}, \tag{23}$$

where M_{ij}^k represents the cell center values at (x_i, y_j) defined for the level-k grid on the domain Ω_{l+k}. Then, we tag the cells containing the interface where the undivided gradient of the order parameter is greater than a tolerance ε, i.e., $|\nabla_u M|^k > \varepsilon$. Throughout this paper, we use $\varepsilon = 0.01$. After determining the cells that need to be refined, the algorithm of Berger and Rigoutsos [39] is used to tag points that are clustered into efficient boxes. The ghost-layer values are then obtained by using quadratic interpolation based on the previous level data. For further details, refer to Refs. [37,38].

3.2. Numerical solution – adaptive nonlinear multigrid method

Here, we briefly describe the adaptive nonlinear multigrid procedure for solving the nonlinear discrete system of Eqs. (9) and (10). First, we recast the equations as $N(\mathbf{c}^{n+1}, \mu^{n+1}) = (\phi^n, \psi^n)$, where $N(\mathbf{c}^{n+1}, \mu^{n+1}) = (\mathbf{c}^{n+1}/\Delta t - \nabla_d \cdot (\hat{M}(\mathbf{c}^n)\nabla_d \mu^{n+1}), \mu^{n+1} - g(\mathbf{c}^{n+1}) + \epsilon^2 \Delta_d \mathbf{c}^{n+1})$ and the source term is given as $(\phi^n, \psi^n) = (\mathbf{c}^n/\Delta t, -0.25\mathbf{c}^n + \hat{\beta}(\mathbf{c}^n)\mathbf{1})$. Here, $g(\mathbf{c}^{n+1}) = f(\mathbf{c}^{n+1}) + 0.25\mathbf{c}^{n+1}$. Then, the relaxation operator step can be written in 2×2 matrix-vector form for each i and j as follows:

$$\frac{c_{r,ij}^{n+1}}{\Delta t} + \frac{\hat{M}_{i+\frac{1}{2},j}^n + \hat{M}_{i-\frac{1}{2},j}^n + \hat{M}_{i,j+\frac{1}{2}}^n + \hat{M}_{i,j-\frac{1}{2}}^n}{h^2} \mu_{r,ij}^{n+1} = \phi_{r,ij}^n$$

$$+ \frac{\hat{M}_{i+\frac{1}{2},j}^n \mu_{r,i+1,j}^{n+1} + \hat{M}_{i-\frac{1}{2},j}^n \mu_{r,i-1,j}^{n+1} + \hat{M}_{i,j+\frac{1}{2}}^n \mu_{r,i,j+1}^{n+1} + \hat{M}_{i,j-\frac{1}{2}}^n \mu_{r,i,j-1}^{n+1}}{h^2}, \tag{24}$$

$$-\frac{4\epsilon^2}{h^2} c_{r,ij}^{n+1} - g(c_{r,ij}^{n+1}) + \mu_{r,ij}^{n+1} = \psi_{r,ij}^n - \epsilon^2 \frac{c_{r,i+1,j}^{n+1} + c_{r,i-1,j}^{n+1} + c_{r,i,j+1}^{n+1} + c_{r,i,j-1}^{n+1}}{h^2}. \tag{25}$$
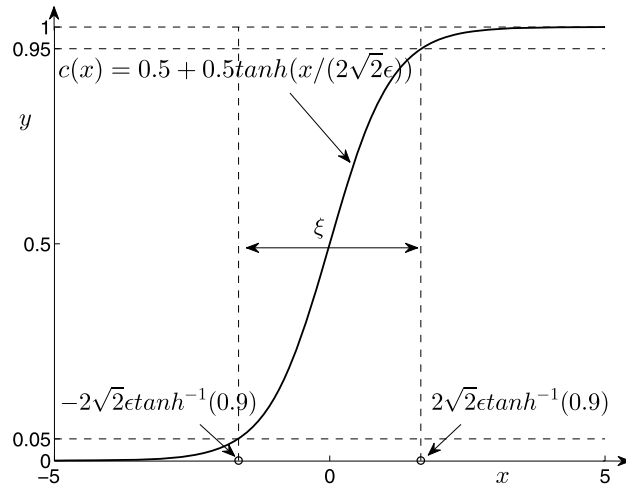
Fig. 5. Equilibrium concentration profile in an interfacial region.

Next, the pointwise Gauss–Seidel relaxation scheme is used as a smoother in the multigrid method. We replace $c_{r,pq}^{n+1}$ and $\mu_{r,pq}^{n+1}$ in Eqs. (24) and (25) with $\bar{c}_{r,pq}^{m}$ and $\bar{\mu}_{r,pq}^{m}$ if $p \leq i$ and $q \leq j$; otherwise, we replace them with $c_{r,pq}^{m}$ and $\mu_{r,pq}^{m}$. Thus, Eqs. (9) and (10) yield

$$
\frac{\bar{c}_{r,ij}^{m}}{\Delta t} + \frac{\hat{M}_{i+\frac{1}{2},j}^{n} + \hat{M}_{i-\frac{1}{2},j}^{n} + \hat{M}_{i,j+\frac{1}{2}}^{n} + \hat{M}_{i,j-\frac{1}{2}}^{n}}{h^2} \bar{\mu}_{r,ij}^{m} = \phi_{r,ij}^{n}
$$

$$
+ \frac{\hat{M}_{i+\frac{1}{2},j}^{n} \mu_{r,i+1,j}^{m} + \hat{M}_{i-\frac{1}{2},j}^{n} \bar{\mu}_{r,i-1,j}^{m} + M_{i,j+\frac{1}{2}}^{n} \mu_{r,i,j+1}^{m} + \hat{M}_{i,j-\frac{1}{2}}^{n} \bar{\mu}_{r,i,j-1}^{m}}{h^2}, \tag{26}
$$

$$
-\frac{4\epsilon^2}{h^2} \bar{c}_{r,ij}^{m} - g(\bar{c}_{r,ij}^{m}) + \bar{\mu}_{r,ij}^{m} = \psi_{r,ij}^{n} - \epsilon^2 \frac{c_{r,i+1,j}^{m} + \bar{c}_{r,i-1,j}^{m} + c_{r,i,j+1}^{m} + \bar{c}_{r,i,j-1}^{m}}{h^2}. \tag{27}
$$

Since $g(\bar{c}_{r,ij}^{m})$ is nonlinear with respect to $\bar{c}_{r,ij}^{m}$, we linearize $g(\bar{c}_{r,ij}^{m})$ at $c_{r,ij}^{m}$ as

$$
g(\bar{c}_{r,ij}^{m}) = g(c_{r,ij}^{m}) + g'(c_{r,ij}^{m})(\bar{c}_{r,ij}^{m} - c_{r,ij}^{m}). \tag{28}
$$

Using Eq. (28), Eq. (27) yields

$$
\left(-g'(c_{r,ij}^{m}) - \frac{4\epsilon^2}{h^2} \right) \bar{c}_{r,ij}^{m} + \bar{\mu}_{r,ij}^{m}
$$

$$
= \psi_{r,ij}^{n} + g(c_{r,ij}^{m}) - g'(c_{r,ij}^{m}) c_{r,ij}^{m} - \epsilon^2 \frac{c_{r,i+1,j}^{m} + \bar{c}_{r,i-1,j}^{m} + c_{r,i,j+1}^{m} + \bar{c}_{r,i,j-1}^{m}}{h^2}, \tag{29}
$$

where $g'(c_{r,ij}^{m})$ is the first derivative of $g(c_{r,ij}^{m})$. This completes the pointwise Gauss–Seidel relaxation. Similarly, the adaptive nonlinear multigrid procedure can be applied for solving other CH systems in Eqs. (3) and (4), and Eqs. (15) and (16). For details of the adaptive V-cycle multigrid method, refer to Refs. [37,38].

4. Numerical experiments

This section discusses the numerical experiments that we performed for spinodal decomposition, stability and accuracy tests of the proposed scheme, comparison between uniform and adaptive mesh, and multi-component Cahn–Hilliard system with background fluid. We assume an equilibrium profile, $c(x) = 0.5 + 0.5 \tanh(x/(2\sqrt{2}\epsilon))$ in an infinite domain. Across an interfacial region, the phase concentration varies from 0.1 to 0.9 over a distance of approximately $\xi = 4\sqrt{2}\epsilon \tanh^{-1}(0.9)$, as shown in Fig. 5. Thus, ϵ can be determined as $\epsilon = \epsilon_m = mh/[4\sqrt{2}\tanh^{-1}(0.9)]$ such that ξ is around m grid points in the interfacial transition layer.

4.1. Spinodal decomposition

Spinodal decomposition is a mechanism by which a solution of two or more components separates into different phases. The system separates into spatial regions that are rich in one species and poor in the other species, and
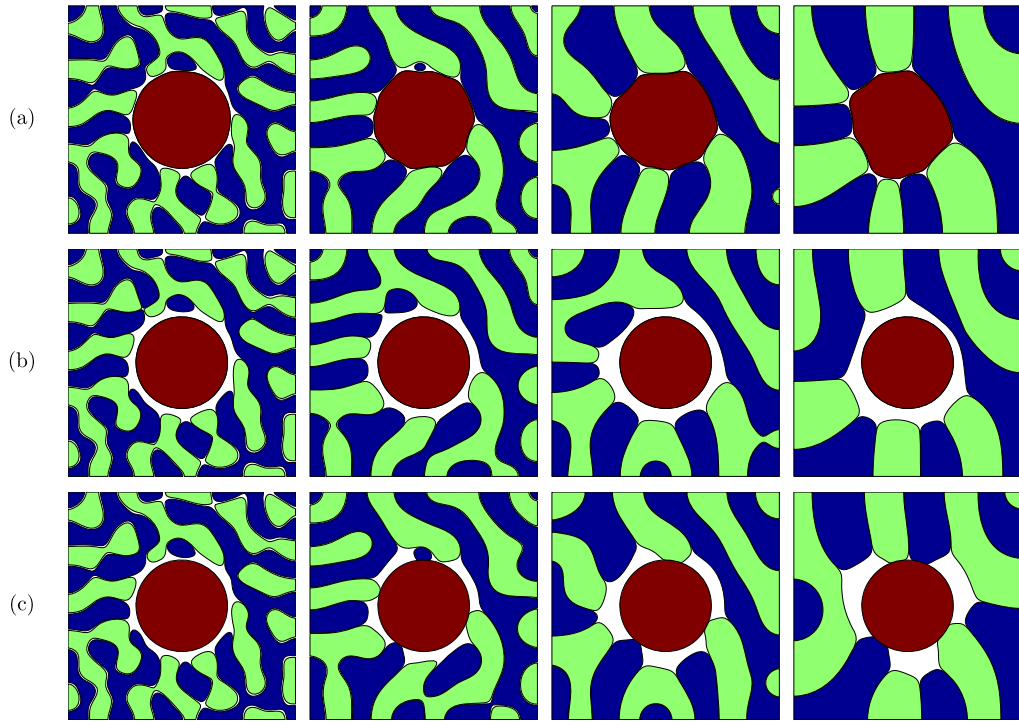
Fig. 6. Spinodal decomposition of a multi-phase mixture. (a) Four components in a rectangular domain: the circle-shaped phase is set as a liquid and can be mixed with other phases. (b) Three components with a solid region treated with no mass flow boundary condition. (c) Three components with Neumann boundary condition. From left to right, the snapshots are taken at $t = 0.391,\ 1.953,\ 7.813$, and 39.062.

evolves into an equilibrium state with a lower overall free energy [2,26]. Here, we consider a case of four components in a rectangular domain $[0, 1] \times [0, 1]$ and two cases of a circular solid region where a no mass flow boundary condition or Neumann boundary condition is imposed. The initial conditions in the first case are set to $c_3(x, y, 0) = 0.5 + 0.5 \tanh((0.2 - \sqrt{(x - 0.5)^2 + (y - 0.5)^2})/(2\sqrt{2}\epsilon))$, $c_1(x, y, 0) = (0.4 + 0.1\ rand(x, y))(1 - c_3(x, y, 0))$, and $c_2(x, y, 0) = (0.4 + 0.1\ rand(x, y))(1 - c_3(x, y, 0))$. Here, $rand()$ denotes a random function that generates a value from -1 to 1. The solid phase in the other two cases is set to $c_0 = c_3$ and the other components are defined in the same ways as those in the first case. We use $h = 1/128$ and $\epsilon = \epsilon_5$. Simulations are run up to time $T = 39.062$ with time step $\Delta t = h$. Fig. 6 shows the evolution of spinodal decomposition for the three cases. For the four-component case, Fig. 6 (a) shows that the phases are well mixed as time proceeds. As shown in Fig. 6 (b), for the case of a solid region with a no mass flow boundary condition, the liquid phases are well mixed with each other, but the no mass flow boundary condition at the solid surface makes the liquid phases completely separated from the solid region for a long time evolution period. However, the Neumann boundary condition enables the liquid phases to maintain a contact angle of $90°$ on the boundary (see Fig. 6 (c)).

We also perform numerical simulations of spinodal decomposition with a fairly large time step $\Delta t = 10$ in order to show the stability of the proposed method. The order parameters (c) after ten iterations for the three cases are shown in Fig. 7. In all the cases, the maximum amplitudes are bounded and the numerical solutions do not blow up during the computation. This indicates that the proposed method provides stable numerical solutions with a fairly large time step.

Further, we investigate the robustness of the proposed method with AMR for simulating spinodal decomposition. The four-level grid refinement ($l^* = 4$) is considered in the unit domain, where the minimum grid spacing is $h_{min} = 1/1024$. The computational time step and interface transition layer are set to $\Delta t = 0.002$ and $\epsilon = 0.01$, respectively. Fig. 8 shows the phase distributions along with the corresponding hierarchical grid at $t = 10$ for the proposed method with no mass flow and Neumann boundary conditions. The spinodal decomposition patterns depend on the imposed boundary condition while maintaining the volumes of the initial phases. As shown in Figs. 8 (c) and (d), the proposed grid refinement technique based on the criteria in Eq. (23) provides appropriate grid resolutions near the phase interfaces. This indicates that the proposed method with two different boundary conditions has been properly implemented with AMR for simulating spinodal decomposition of multi-component phases.

4.2. Accuracy of the proposed scheme

Here, we consider two problems to show the accuracy of the proposed scheme. The first is linear stability analysis in a rectangular domain and the second is an equilibrium phase interface contacting a solid boundary.
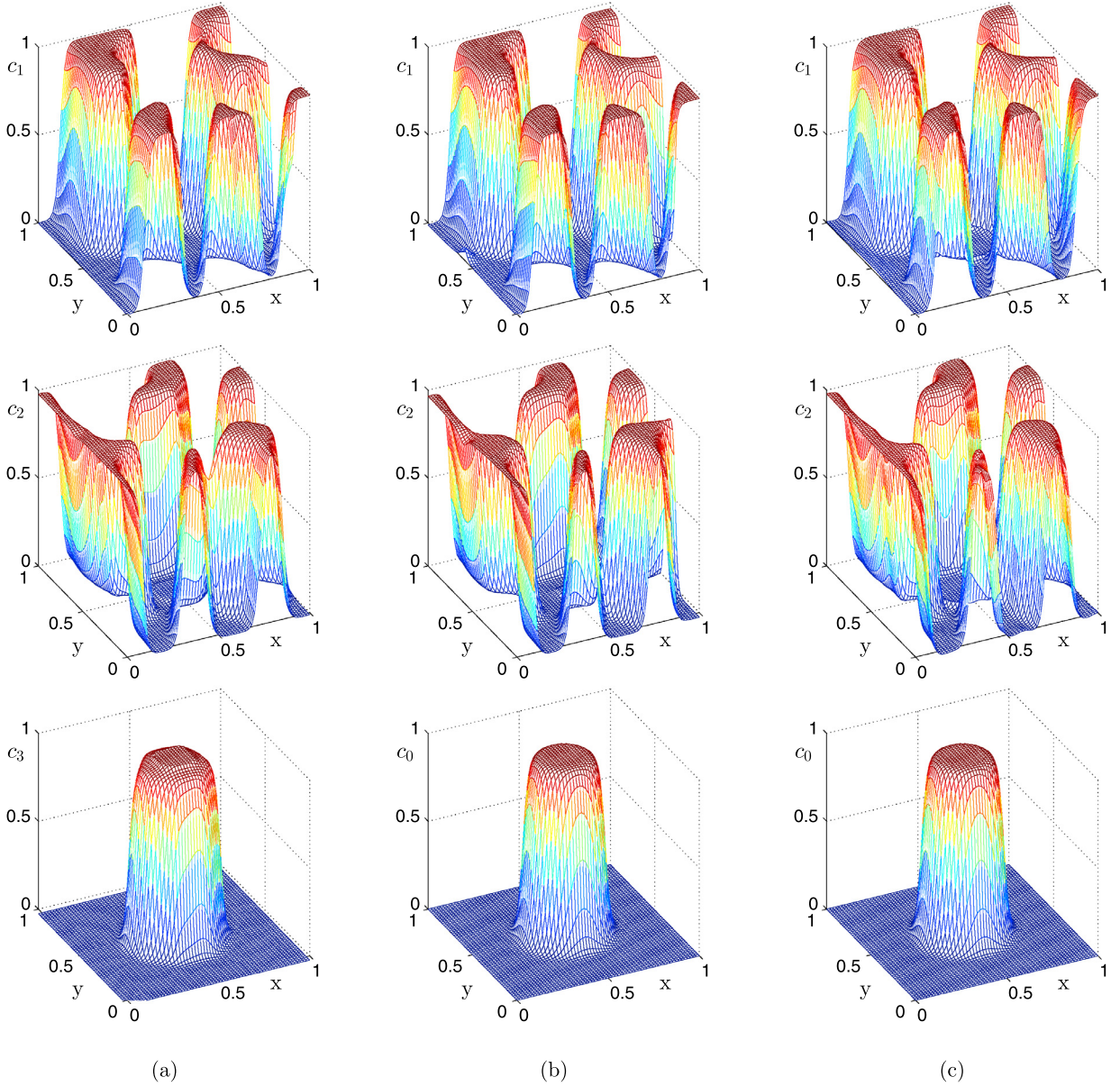
Fig. 7. Mesh plots of order parameters (c) after ten iterations. Here, a fairly large computational time step $\Delta t = 10$ is used. (a) Four components with a circle-shaped phase and three components with a solid region treated with (b) no mass flow boundary condition and (c) Neumann boundary condition.

4.2.1. Linear stability analysis

Linear stability analysis is an effective means for showing the accuracy of the multi-phase CH system. Here, we consider it with four compounds in one-dimensional space. For simplicity, we set $M = 1$. In Refs. [21] and [22], the authors have shown that the solutions of a four-component CH system are given as

$$\mathbf{c}(x, t) = \mathbf{m} + \sum_{k=1}^{\infty} \cos(k\pi x)(\alpha_k(t), \beta_k(t), \gamma_k(t))$$

on the domain $\Omega = (0, 1)$. Here, $\mathbf{m} = (m, m, m)$, where m is a positive value, and $\alpha_k(t)$, $\beta_k(t)$, and $\gamma_k(t)$ take the following form:

$$(\alpha_k(t), \beta_k(t), \gamma_k(t)) = \frac{\alpha_k(0) + \beta_k(0) + \gamma_k(0)}{3} (1, 1, 1) e^{\lambda_1 t}$$
$$+ \frac{-\alpha_k(0) - \beta_k(0) + 2\gamma_k(0)}{3} (-1, 0, 1) e^{\lambda_2 t}$$
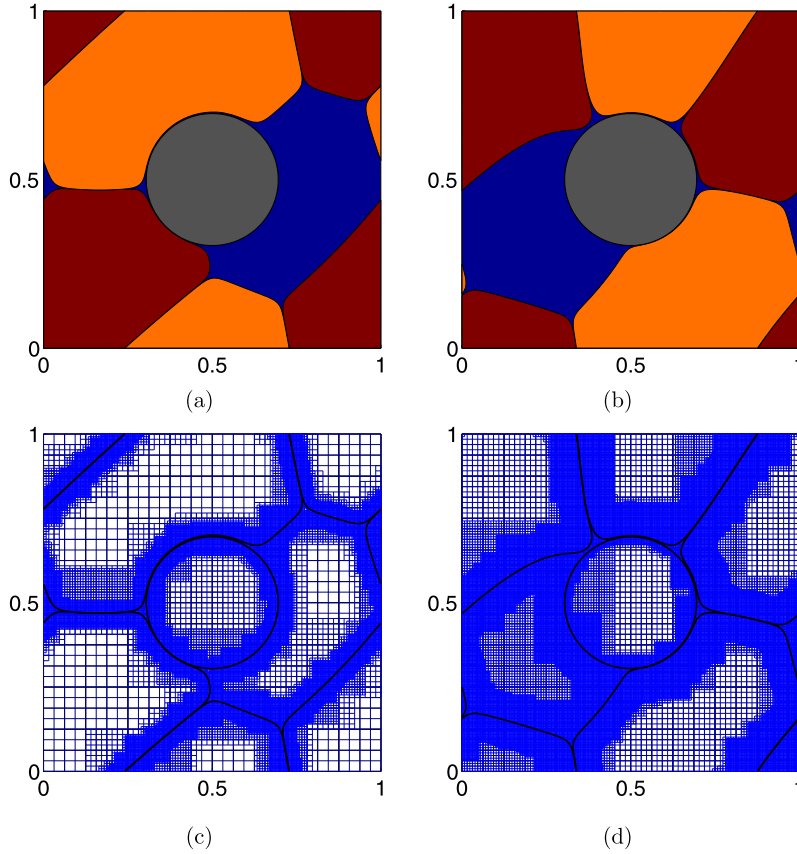
Fig. 8. Simulations of spinodal decomposition with AMR. Here, a circular solid is located at the center of the domain, with radius 0.2. Contour plots of phase distributions from numerical simulations with (a) no mass flow and (b) Neumann boundary conditions along with the corresponding adapted meshes (c) and (d), respectively. Note that for better visualization, the mesh plots in (b) and (d) are displayed at one-fourth of the actual density.

$$+ \frac{-\alpha_k(0) + 2\beta_k(0) - \gamma_k(0)}{3} (-1, 1, 0) e^{\lambda_3 t},$$

where

$$\lambda_1 = -\frac{k^2\pi^2}{2}(42m^2 - 15m + 1 + 2\epsilon^2 k^2\pi^2)$$

$$\lambda_2 = \lambda_3 = -\frac{k^2\pi^2}{2}(6m^2 - 6m + 1 + 2\epsilon^2 k^2\pi^2).$$

The initial conditions are set to $c_1(x, 0) = 0.24 + 0.1\cos(2\pi x)$, $c_2(x, 0) = 0.24 + 0.2\cos(2\pi x)$, and $c_3(x, 0) = 0.24 + 0.3\cos(2\pi x)$. The simulation is run up to $T = 0.1$ with time step $\Delta t = 0.1h$. Here, $h = 1/128$ and $\epsilon = \epsilon_5$ are used. Furthermore, the numerical definition of α, β, and γ are as follows:

$$\alpha^n = \left(\max_{1 \le i \le N_x} c_1^n(x_i) - \min_{1 \le i \le N_x} c_1^n(x_i) \right) / 2$$

$$\beta^n = \left(\max_{1 \le i \le N_x} c_2^n(x_i) - \min_{1 \le i \le N_x} c_2^n(x_i) \right) / 2$$

$$\gamma^n = \left(\max_{1 \le i \le N_x} c_3^n(x_i) - \min_{1 \le i \le N_x} c_3^n(x_i) \right) / 2.$$

Fig. 9 shows that the present numerical solutions of α, β, and γ are in good agreement with the theoretical solutions.

4.2.2. Equilibrium contact angles

To show the accuracy of the proposed method defined in Eqs. (15) and (16) for a complex domain, we consider an equilibrium phase interface contacting a solid with a prescribed contact angle θ. The solid (c_0) and initial compound (c_1) are defined as
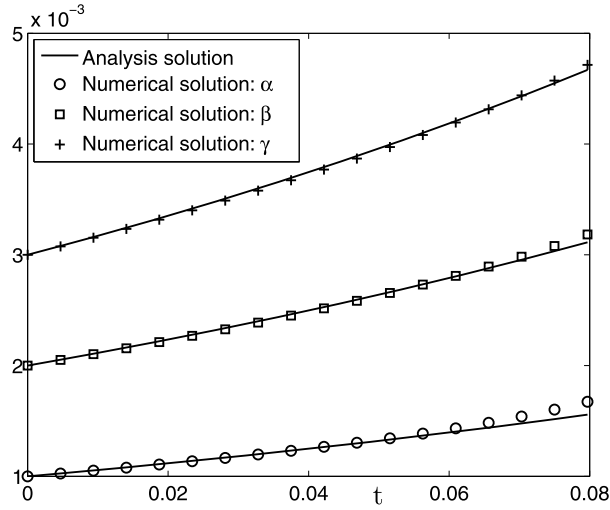
Fig. 9. Comparisons of numerical solutions with analysis solution.
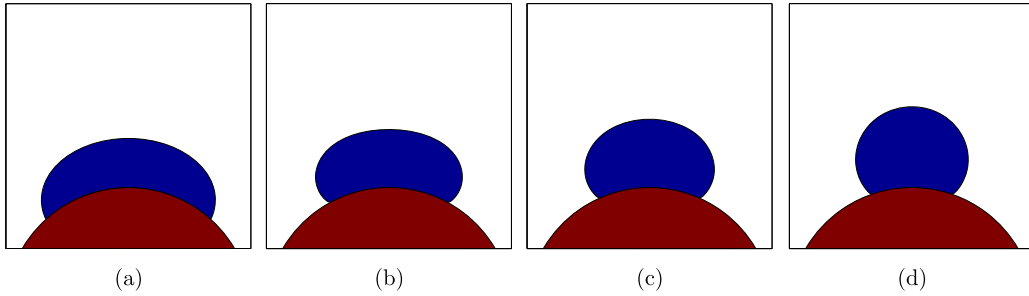
Fig. 10. Evolution of phase interface contacting a solid boundary. (a) $t = 0$ (initial condition), (b) $t = 3.125$, (c) $t = 6.250$, and (d) $t = 14.063$ (equilibrium condition).

$$c_0(x, y) = 0.5 + 0.5 \tanh \left(\frac{0.5 - \sqrt{(x - 0.5)^2 + (y + 0.25)^2}}{2\sqrt{2}\epsilon} \right), \tag{30}$$

$$c_1(x, y) = \begin{cases} 1 - c_0(x, y) & \text{if } c_0(x, y) + \psi(x, y) > 1, \\ \psi(x, y) & \text{otherwise,} \end{cases} \tag{31}$$

where

$$\psi(x, y) = 0.5 + 0.5 \tanh \left(\frac{0.25 - \sqrt{(x - 0.5)^2 + (y - 0.2)^2}}{\sqrt{2}\epsilon} \right). \tag{32}$$

We consider the computational domain $\Omega = (0, 1) \times (0, 1)$ with a 256×256 mesh. Numerical simulations with computational time step $\Delta t = 0.5h$ are performed until an equilibrium condition is obtained. The equilibrium condition is determined by a convergence criterion based on $||(c_1^{n+1} - c_1^n)||_2/||c_1^n||_2 \leq 10^{-6}$.

Fig. 10 shows a typical evolution of the liquid phase c_1 from the initial condition to the equilibrium condition. The theoretical contact angle is given as $\theta = 60°$, while the contact angle is initially set to $\theta \approx 120°$. The proposed method clearly predicts that the phase interface contacting the solid boundary approaches the equilibrium condition with the theoretical contact angle.

To quantify the accuracy of the proposed model, we perform numerical simulations of the equilibrium contact angle problem considering different theoretical (or prescribed) contact angles $\theta = 45°$, $60°$, $90°$, and $135°$. Two grids (256×256 and 512×512) are used for this analysis with computational time step $\Delta t = 0.5h$. Table 1 indicates that with a better grid resolution, the contact angle under the equilibrium condition is predicted with greater accuracy. Overall, the proposed model shows good agreement between the theoretical contact angles and numerical results [4], which confirms that the model accurately captures phase interfaces in a complex domain.

Table 1
Numerical results of contact angles under the equilibrium condition for different theoretical contact angles and mesh sizes. Here, for comparison of our results with the numerical results [4], we show them together. Note that the numerical tests [4] are performed in a rectangular domain, while our tests are performed in the complex domain.

Case	Grid	Theoretical contact angle (°)			
		$\theta = 45°$	$\theta = 60°$	$\theta = 90°$	$\theta = 135°$
Complex domain	256×256	47.445	63.544	91.032	132.564
	512×512	46.124	61.758	90.017	133.346
Rectangular domain [4]	256×128	43.969	60.893	90.842	135.593
	512×256	44.245	60.683	90.421	135.284
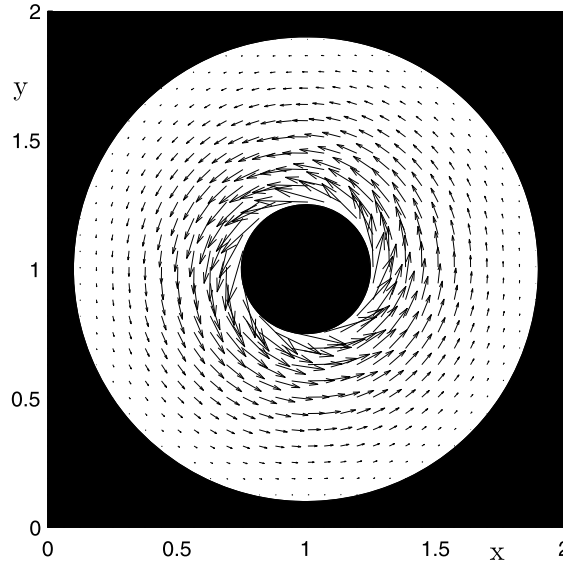
Fig. 11. Velocity field in Taylor–Couette cell.

4.3. Multi-component CH system with background fluid

To verify the robustness of the proposed CH system in a complex domain, we consider an advection CH system where the phase interfaces can be advected with the given background velocity field **u**. The corresponding advection CH equation can be written as

$$\frac{\partial c_i}{\partial t} + \nabla \cdot (\mathbf{u} c_i) = \frac{1}{Pe} \nabla \cdot (M(\mathbf{c}) \nabla \mu_i), \tag{33}$$

where Pe is a positive parameter. In the present study, background velocity fields have been prescribed on the basis of theoretical analysis or determined *a priori* by using the immersed boundary method in a Cartesian grid [29]. Based on the velocity fields in the Cartesian mesh, quadratic interpolation is applied to obtain velocity fields at adaptive meshes to solve the advection CH equation, i.e., Eq. (33). It should be noted that the AMR framework is used only for the multi-component CH system.

4.3.1. Multi-component Cahn–Hilliard system for Taylor–Couette cell

We consider the shear-driven spinodal decomposition occurring in a Taylor–Couette cell, where incompressible fluid is trapped between two concentric cylinders [40]. For the Taylor–Couette flow, we assume that the inner cylinder is rotating, and the outer cylinder is fixed. The computational domain is defined as a ring-type domain where the radii of the inner and outer cylinders are set to 0.25 and 0.9, respectively. The background velocity field in Fig. 11 is given as

$$\mathbf{u} = (u, v) = \left(\frac{0.0676}{(x-1)^2 + (y-1)^2} - 0.0734 \right) (1-y, x-1). \tag{34}$$

Two types of phase boundary conditions (Neumann and no mass flow boundary conditions) are applied to both the inner cylinder and the outer cylinder. The initial condition is set to $c_1(x, y, 0) = 0.5 + 0.1 \, rand(x, y)$. The five-level grid refinement ($l^* = 5$) is considered in the unit domain, where the minimum and maximum grid spacings are $h_{min} = 1/1024$ and $h_{max} = 1/32$, respectively. The other numerical parameters are set as follows: $\epsilon = 0.01$, $\Delta t = 0.002$, and $Pe = 1$.
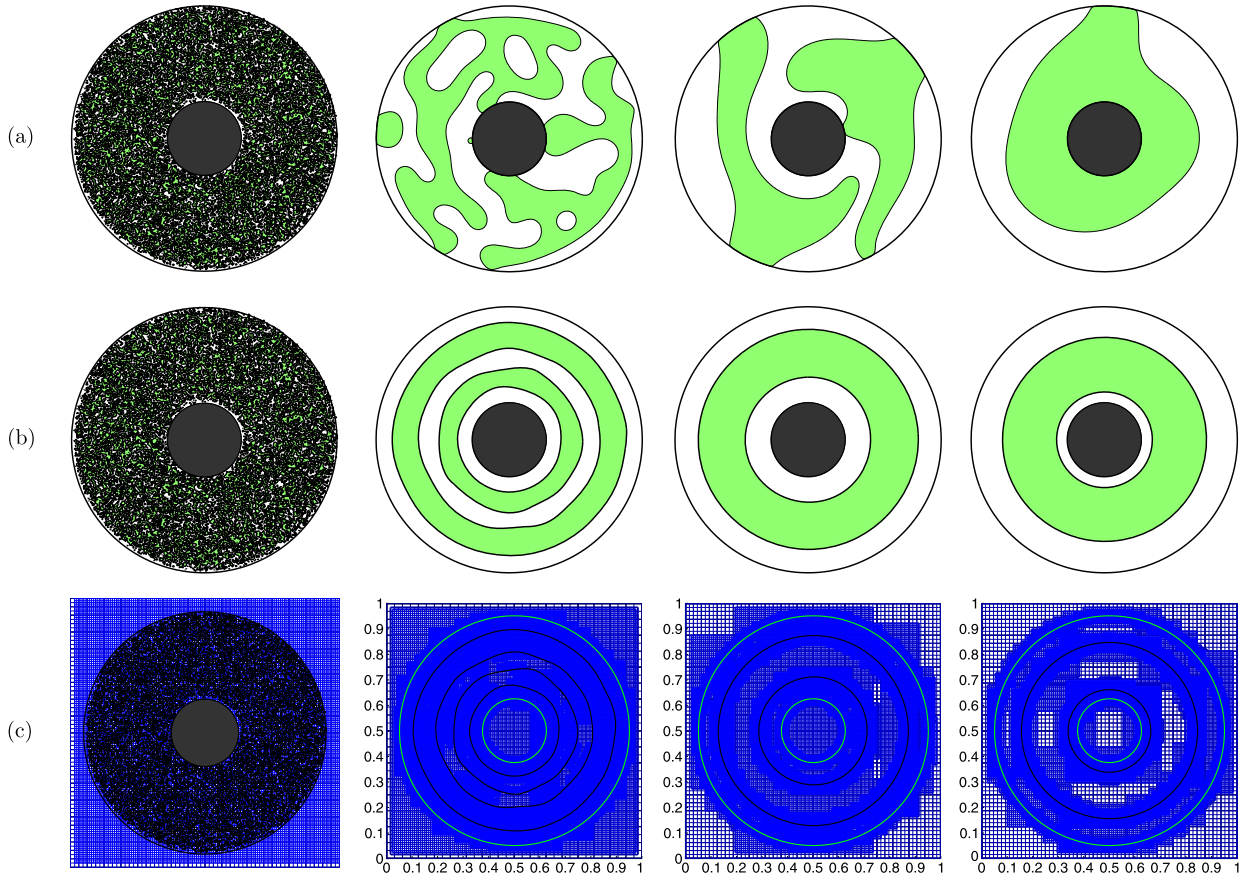
Fig. 12. Spinodal decomposition occurring in a Taylor–Couette cell. Contour plots of phase distributions from numerical simulations with (a) Neumann boundary condition and (b) no mass flow boundary condition along with (c) the corresponding adaptive meshes. From left to right, the computational times are $t = 0$, 0.5, 2.5, and 7.5.
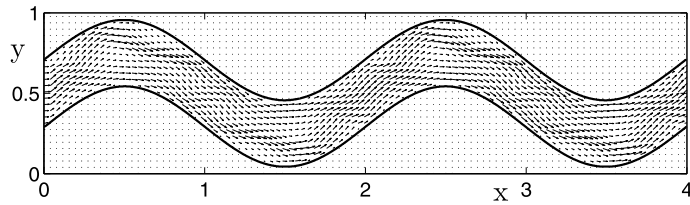
Fig. 13. Velocity field in a wavy channel.

Fig. 12 shows the spinodal decomposition occurring in the Taylor–Couette cell with two-component phase. Since the velocity near the inner cylinder is higher than that near the outer one, the phases are more separated away from the inner cylinder. As time proceeds, the two phases become completely separated, forming two circular bands in the cylinder. Interestingly, the no mass flow boundary condition on the solid boundary results in faster phase separation compared to the Neumann boundary condition.

4.3.2. Multi-component CH system in a wavy channel

The proposed model is tested through numerical simulations of multi-phase flows interacting with complex channel boundaries. The channel geometry is modeled by two sine functions with a period of 2 in the streamwise direction and an amplitude of 0.25. The vertical gap in the channel is set to 0.4. The computational domain is defined as $\Omega = (0, 4) \times (0, 1)$. Using the immersed boundary method [29], the background velocity field is obtained by solving the Navier–Stokes equation with the no-slip Dirichlet boundary condition at a Reynolds number of 10 in a uniform grid of size 1024×256. At the inlet, a parabolic velocity profile is assumed as $\mathbf{u}(0, y) = (-25(y - 0.7)(y - 0.3), 0)$. The corresponding flow field is shown in Fig. 13.
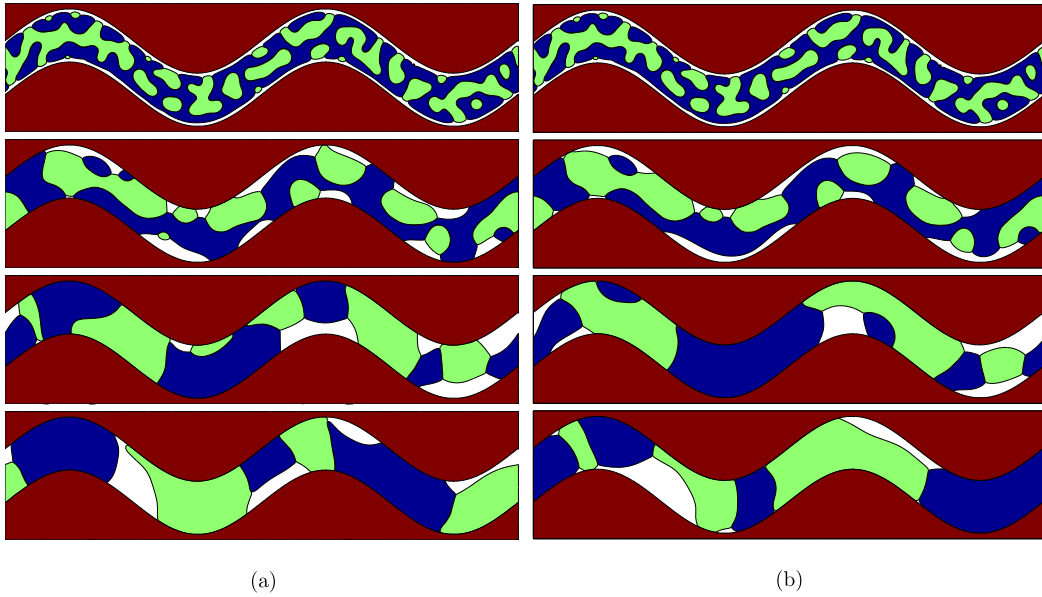
Fig. 14. Multi-phase separations in a wavy channel. Numerical simulations with (a) Neumann boundary condition and (b) no mass flow boundary condition. From top to bottom, the computational times are $t = 0$, 1.5, 4.5, and 15.0.
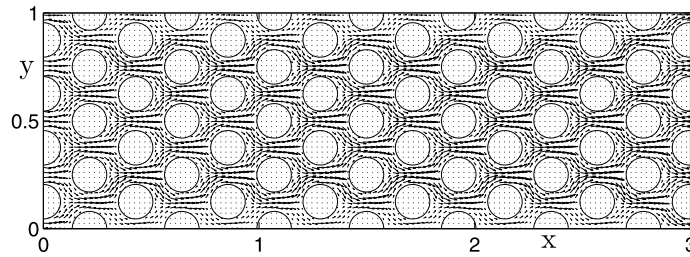
Fig. 15. Flow field in a porous medium.

We conduct numerical simulations of time-varying three-component multi-phase separations with adaptive mesh refinement in a wavy channel for the given multi-phase distributions. Here, the five-level grid refinement ($l^* = 5$) is considered in the same computational domain. The level zero domain (Ω_{l+0}) is discretized with a uniform grid of size 64×16, while the minimum grid spacing $h_{min} = 1/512$ is used for the level l^* domain (Ω_{l+l^*}). The computational time step and interface transition layer are set to $\Delta t = 0.002$ and $\epsilon = 0.01$, respectively. Periodic boundary conditions are applied to the multi-component phase at the inlet and outlet. Figs. 14 (a) and (b) show the evolutions of droplets in the wavy channel at $t = 0$, 1.5, 4.5, and 15.0 for numerical simulations with Neumann and no mass flow boundary conditions, respectively. The results indicate that the length scale of the phases tends to be larger than the initial length scale owing to the phase separation and merging process as the phases move through the channel. Depending on the boundary condition, the dynamic evolutions of multi-phases differ. The no mass flow boundary condition seems to provide a slightly faster phase separation (or merging) than the Neumann boundary condition.

4.3.3. Multi-component Cahn–Hilliard system in a porous medium

Transport phenomena in porous media play an important role in many fields such as hydrology and petroleum engineering. Recently, a phase-field modeling approach has attracted considerable attention in the study of transport phenomena in a porous medium because of its ability to accurately predict flow physics involving sophisticated moving interfaces and complex topologies [41]. Here, we consider two phase flows in a modeled porous medium, as shown in Fig. 15. The background flow field, as shown in Fig. 15, is obtained *a priori* by using the immersed boundary method [29] to solve the incompressible Navier–Stokes equation with the no-slip Dirichlet boundary condition on the solid surface. The computational domain is defined as $\Omega = (0, 3) \times (0, 1)$ with a uniform grid (768×256). Here, we set the Reynolds number to 2 on the basis of the channel height and bulk velocity.

Based on the background flow field, we carry out numerical simulations of the two phase flows in the porous medium by solving the multi-component CH system. We consider the four-level grid refinement ($l^* = 4$), where the maximum and minimum grid sizes are $h_{max} = 1/32$ and $h_{min} = 1/512$, respectively. The other numerical parameters are set as follows:
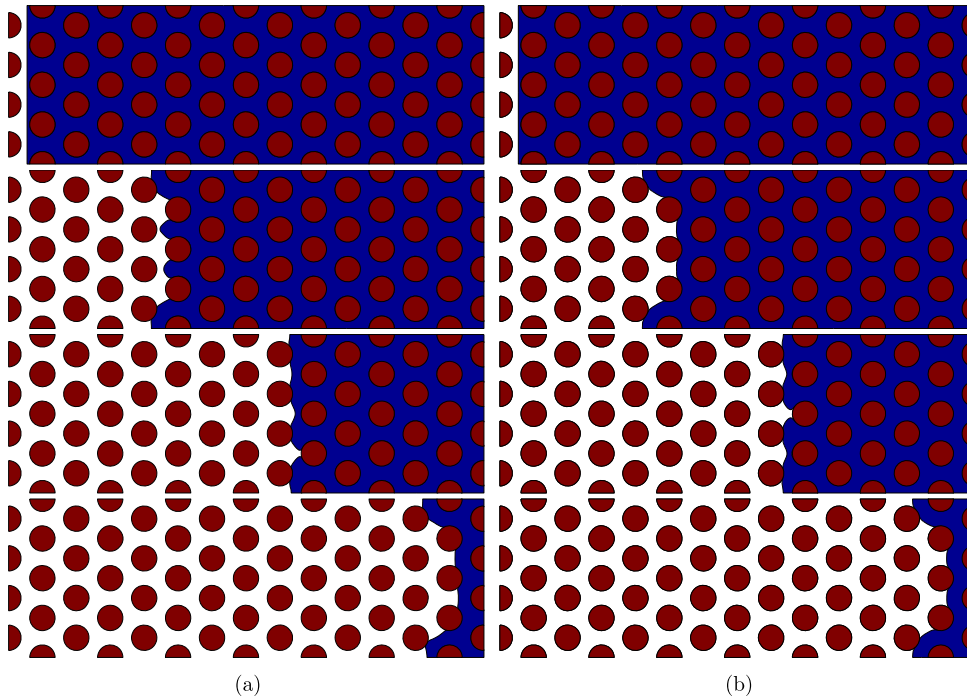
Fig. 16. Multi-component CH system in a porous medium. Numerical simulations with (a) Neumann boundary condition and (b) no mass flow boundary condition. From top to bottom, the computational times are $t = 0$, 1.8, 3.6, and 4.8. Note that the two phases are represented in black and white.

$\Delta t = 0.002$, $\epsilon = 0.01$, and $Pe = 0.1$. Fig. 16 shows that the proposed method with Neumann or no mass flow boundary conditions provides evolutions of the phase separations interacting with the immersed pore-like obstacles in the wavy channel. Although the transient behaviors of the phase evolutions are slightly different near the obstacles depending on the boundary condition, the overall characteristics of the time-dependent phase advection are similar for both the boundary conditions.

5. Conclusions

We proposed an efficient phase-field model for multi-component CH systems with different boundary conditions in complex domains. Considering the complex domain as a fixed phase, the original multi-component CH system was modified to accurately predict phases near the domain boundaries by proper boundary treatment in the Cartesian grid. Two different boundary conditions (no mass flow and contact angle boundary conditions) were applied to resolve the complex domain boundaries. The chemical potential in the CH system was also recast on the basis of a hyperbolic tangent profile for the equilibrium interface at the boundaries, satisfying the surface energy formulation based on Young's equation. For the fixed phase, a diffusion deformable interface approach was considered in a discrete domain, which is more suitable for the AMR framework. The multi-component CH system was formulated semi-implicitly with a practically unconditionally gradient stable nonlinear splitting numerical scheme in order to eliminate the high-order time step stability constraints. The resulting nonlinear discrete equations were then solved using a nonlinear full approximation storage multigrid algorithm. We carried out numerical simulations of phase separations via spinodal decomposition to assess the proposed method under the two above-mentioned boundary conditions in the AMR framework. Further, the accuracy of the proposed method was investigated via comparisons with linear stability analysis and estimations of equilibrium contact angles with complex boundaries. The numerical results confirmed that the proposed method accurately captures phase interfaces as compared to the theoretical estimates. In addition, we demonstrated the robustness of the proposed method for simulating multi-phase flows with a background fluid in a complex domain.

Acknowledgements

References

[1] J.W. Cahn, J.E. Hilliard, Free energy of a nonuniform system. I. Interfacial free energy, J. Chem. Phys. 28 (1958) 258–267.

[2] J.W. Cahn, On spinodal decomposition, Acta Metall. 9 (1961) 795–801.

[3] R. Chella, J. Viñals, Mixing of a two-phase fluid by cavity flow, Phys. Rev. E 53 (1996) 3832–3840.

[4] H.G. Lee, J.S. Kim, Accurate contact angle boundary conditions for the Cahn–Hilliard equations, Comput. Fluids 44 (2011) 178–186.

[5] W. Jiang, W. Bao, C.V. Thompson, D.J. Srolovitz, Phase field approach for simulating solid-state dewetting problems, Acta Mater. 60 (15) (2012) 5578–5592.

[6] H. Ding, D.D.M. Spelt, C. Shu, Diffuse interface model for incompressible two-phase flows with large density ratios, J. Comput. Phys. 226 (2007) 2078–2095.

[7] J. Kim, Phase field computations for ternary fluid flows, Comput. Methods Appl. Mech. Eng. 196 (45–48) (2007) 4779–4788.

[8] J. Kim, A generalized continuous surface tension force formulation for phase-field models for immiscible multi-component fluid flows, Comput. Methods Appl. Mech. Eng. 198 (2009) 3105–3112.

[9] Y. Li, J.-I. Choi, J. Kim, A phase-field fluid modeling and computation with interfacial profile correction term, Commun. Nonlinear Sci. Numer. Simul. 30 (2016) 84–100.

[10] S. Wise, J. Lowengrub, H. Frieboes, V. Cristini, Three-dimensional multispecies nonlinear tumor growth: I. Model and numerical method, J. Theor. Biol. 253 (2008) 524–543.

[11] V. Cristini, X. Li, J.S. Lowengrub, S.M. Wise, Nonlinear simulations of solid tumor growth using a mixture model: invasion and branching, J. Math. Biol. 58 (2009) 723–763.

[12] A. Bertozzi, S. Esedoglu, A. Gillette, Inpainting of binary images using the Cahn–Hilliard equation, IEEE Trans. Image Process. 16 (2007) 285–291.

[13] Y. Li, J. Shin, Y. Choi, J. Kim, Three-dimensional volume reconstruction from slice data using phase-field models, Comput. Vis. Image Underst. 137 (2015) 115–124.

[14] D. de Fontaine, A computer simulation of the evolution of coherent composition variations in solid solutions, Ph.D. Thesis, Northwestern University, 1967.

[15] J.E. Morral, J.W. Cahn, Spinodal decomposition in ternary systems, Acta Metall. 19 (1971) 1037–1045.

[16] J.J. Hoyt, The continuum theory of nucleation in multicomponent systems, Acta Metall. 38 (1990) 1405–1412.

[17] C.M. Elliott, S. Luckhaus, A generalised diffusion equation for phase separation of a multi-component mixture with interfacial free energy, IMA Prepr. Ser. 887 (1991).

[18] D.J. Eyre, Systems of Cahn–Hilliard equations, SIAM J. Appl. Math. 53 (1993) 1686–1712.

[19] C.M. Elliott, H. Garcke, Diffusional phase transitions in multicomponent systems with a concentration dependent mobility matrix, Physica D 109 (1997) 242–256.

[20] S. Maier-Paape, B. Stoth, T. Wanner, Spinodal decomposition for multicomponent Cahn–Hilliard systems, J. Stat. Phys. 98 (2000) 871–896.

[21] H.G. Lee, J. Kim, A second-order accurate non-linear difference scheme for the N-component Cahn–Hilliard system, Physica A 387 (2008) 4787–4799.

[22] H.G. Lee, J.-W. Choi, J. Kim, A practically unconditionally gradient stable scheme for the N-component Cahn–Hilliard system, Physica A 391 (2012) 1009–1019.

[23] D. Calhoun, A Cartesian grid method for solving the two-dimensional streamfunction-vorticity equations in irregular regions, J. Comput. Phys. 176 (2) (2002) 231–275.

[24] H.S. Udaykumar, R. Mittal, P. Rampunggoon, A. Khanna, A sharp interface Cartesian grid method for simulating flows with complex moving boundaries, J. Comput. Phys. 174 (2001) 345–380.

[25] J. Shin, D. Jeong, J. Kim, A conservative numerical method for the Cahn–Hilliard equation in complex domains, J. Comput. Phys. 230 (2011) 7441–7455.

[26] Y. Li, D. Jeong, J. Shin, J. Kim, A conservative numerical method for the Cahn–Hilliard equation with Dirichlet boundary conditions in complex domains, Comput. Math. Appl. 65 (2013) 102–115.

[27] J.-I. Choi, R.C. Oberoi, J.R. Edwards, J.A. Rosati, An immersed boundary method for complex incompressible flows, J. Comput. Phys. 224 (2007) 757–784.

[28] P. Gómez, J. Hernández, J. López, On the reinitialization procedure in a narrow-band locally refined level set method for interfacial flows, Int. J. Numer. Methods Eng. 63 (2005) 1478–1512.

[29] M.-C. Lai, C.S. Peskin, An immersed boundary method with formal second-order accuracy and reduced numerical viscosity, J. Comput. Phys. 160 (2000) 705–719.

[30] H.D. Ceniceros, A.M. Roma, A nonstiff, adaptive mesh refinement-based method for the Cahn–Hilliard equation, J. Comput. Phys. 225 (2007) 1849–1862.

[31] J. Kim, H.-O. Bae, An unconditionally gradient stable adaptive mesh refinement for the Cahn–Hilliard equation, J. Korean Phys. Soc. 53 (2008) 672–679.

[32] R.H. Stogner, G.F. Carey, B.T. Murray, Approximation of Cahn–Hilliard diffuse interface models using parallel adaptive mesh refinement and coarsening with C^1 elements, Int. J. Numer. Methods Eng. 76 (2008) 636–661.

[33] S.M. Wise, J.S. Lowengrub, V. Cristini, An adaptive multigrid algorithm for simulating solid tumor growth using mixture models, Math. Comput. Model. 53 (2011) 1–20.

[34] B. Nestler, A.A. Wheeler, A multi-phase-field model of eutectic and peritectic alloys: numerical simulation of growth structures, Physica D 138 (2000) 114–133.

[35] T. Young, An essay on the cohesion of fluids, Philos. Trans. R. Soc. Lond. 95 (1805) 65–87.

[36] H. Ding, P.D.M. Spelt, Wetting condition in diffuse interface simulations of contact line motion, Phys. Rev. E 75 (2007) 046708.

[37] Y. Li, J. Kim, Phase-field simulations of crystal growth with adaptive mesh refinement, Int. J. Heat Mass Transf. 55 (2012) 7926–7932.

[38] Y. Li, D. Jeong, J. Kim, Adaptive mesh refinement for simulation of thin film flows, Meccanica 49 (2014) 239–252.

[39] M. Berger, I. Rigoutsos, An algorithm for point clustering and grid generation, IEEE Trans. Syst. Man Cybern. 21 (1991) 1278–1286.

[40] J. Liu, L. Dedè, J.A. Evans, M.J. Borden, T.J.R. Hughes, Isogeometric analysis of the advective Cahn–Hilliard equation: spinodal decomposition under shear flow, J. Comput. Phys. 242 (2013) 321–350.

[41] H.A. Akhlaghi Amiri, A.A. Hamouda, Evaluation of level set and phase field methods in modeling two phase flow with viscosity contrast through dual-permeability porous medium, Int. J. Multiph. Flow 52 (2013) 22–34.